ACS Biomaterials SCIENCE & ENGINEERING

pubs.acs.org/journal/abseba

Article

3D Printing Silk Fibroin/Polyacrylamide Triple-Network Composite Hydrogels with Stretchability, Conductivity, and Strain-Sensing Ability as Bionic Electronic Skins

Qianqian Niu, Li Huang, Suna Fan, Xiang Yao, and Yaopeng Zhang*

Cite This: *ACS Biomater. Sci. Eng.* 2024, 10, 3489−3499

Read Online

ACCESS | Metrics & More | Article Recommendations | Supporting Information

ABSTRACT: Electronic skins have received increasing attention due to their great application potential in wearable electronics. Meanwhile, tremendous efforts are still needed for the fabrication of multifunctional composite hydrogels with complex structures for electronic skins via simple methods. In this work, a novel three-dimensional (3D) printing composite hydrogel with stretchability, conductivity, and strain-sensing ability is produced using a one-step photocuring method to achieve a dual-signal response of the electronic skin. The composite hydrogel exhibits a triple-network structure composed of silk microfibers (SMF), regenerated silk fibroin (RSF), and polyacrylamide (PAM). The establishment of triple networks is based on the electrostatic interaction between SMF and RSF, as well as the chemically cross-linked RSF and PAM. Thanks to its specific structure and components, the composite hydrogel possesses enhanced mechanical properties (elastic modulus of 140 kPa, compressive stress of 21 MPa, and compression modulus of 600 kPa) and 3D printability while retaining stretchability and flexibility. The interaction between negatively charged SMF and cations in phosphate-buffered saline endows the composite hydrogel with good conductivity and strain-sensing ability after immersion in a low-concentration (10 mM) salt solution. Moreover, the 3D printing composite hydrogel scaffold successfully realizes real-time monitoring. Therefore, the proposed hydrogel-based ionic sensor is promising for skin tissue engineering, real-time monitoring, soft robotics, and human−machine interfaces.

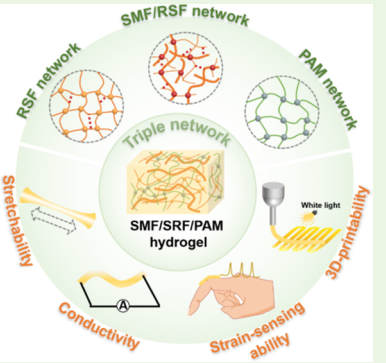

KEYWORDS: *silk fibroin, hydrogel, triple network, strain-sensing ability, 3D printing, electronic skin*

INTRODUCTION

With the development of artificial intelligence, electronic skins have attracted a great deal of attention and achieved remarkable progress in wearable and implantable devices. Hydrogels are considered excellent candidates for electronic skins due to their lightweight, large deformation range, good flexibility, stretchability, and adjustable mechanical properties.[1,2] Moreover, hydrogels are rich in water and ions, which makes them able to record external stimulations according to the activity of the electrons and ions. However, stringent requirements are imposed on the new-generation flexible sensors in terms of mechanical properties, individualized structural design, biocompatibility, and nontoxicity to reduce the risks associated with allergic reactions and inflammatory reactions.[3]

Synthetic polymers, such as polyacrylamide (PAM),[4] poly(acrylic acid),[5] and poly *N*-isopropylacrylamide,[6] are extensively used to prepare hydrogel-based sensors. Compared with synthetic polymers, natural polymers have many advantages, e.g., good biocompatibility, biodegradability, and sustainability. Some natural polymers, like sodium alginate, fibroin, and carrageenan,[7−9] are doped with synthetic polymers to prepare composite hydrogels. Among these natural materials, silk fibroin (SF) derived from silkworm cocoon has abundant sources, low cost, good biodegradability, good biocompatibility, and excellent mechanical properties.[10,11] Thanks to its advantages, SF is widely applied in many fields, such as energy, optics, tissue engineering, and electronic skins.[12−16] The combination of a natural polymer and a synthetic polymer composite hydrogel can provide a synergy of properties, i.e., self-healing and processability of weakly interacting biological materials and strong mechanical properties of the synthetic polymer structure.[17] It is noteworthy that traditional methods of preparation of polymer hydrogels are harsh and laborious. Therefore, it is necessary to develop simple and convenient tools for the fabrication of multifunctional hydrogels.

Hydrogels used in bioelectronics mainly include ionic conductive hydrogels, conducting nanocomposite hydrogels, and conducting polymer hydrogels. Therefore, ionic con-

Received: January 29, 2024
Revised: April 13, 2024
Accepted: April 15, 2024
Published: April 25, 2024

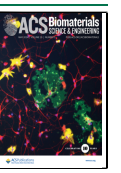

https://doi.org/10.1021/acsbiomaterials.4c00201
ACS Biomater. Sci. Eng. 2024, 10, 3489−3499

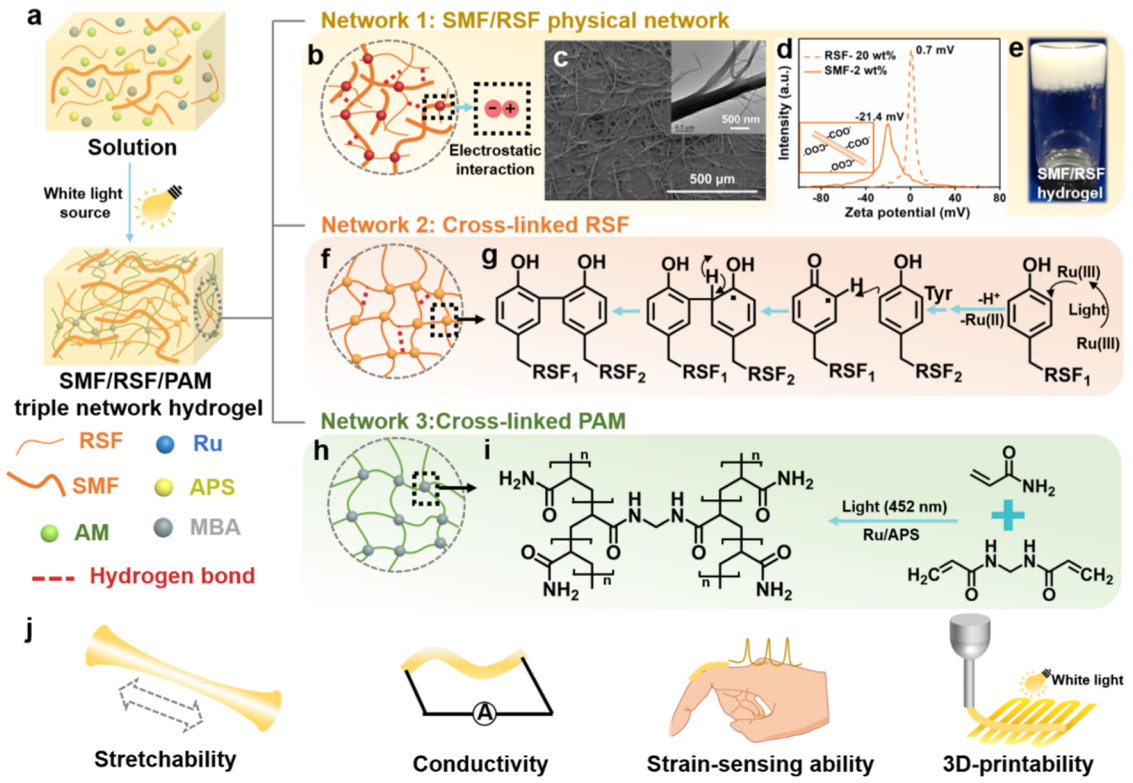

Figure 1. Schematic of the preparation of SMF/RSF/PAM triple-network hydrogels. (a) Synthesis of SMF/RSF/PAM triple-network hydrogels. (b) Electrostatic interaction between RSF and SMF. (c) SEM image of SMF (here, the inset shows the TEM image of SMF). (d) ζ-potential of the SMF suspension and RSF solution (the inset depicts the schematic diagram of negatively charged SMFs). (e) Physical gelation of the RSF/SMF hydrogel. Schematic of (f) cross-linked RSF and (h) cross-linked PAM. Cross-linking of (g) RSF and (i) PAM. (j) Schematic diagram of stretchability, conductivity, strain-sensing ability, and 3D printability of SMF/RSF/PAM hydrogels.

ductive hydrogels realize electrical conductivity through the movement of salt ions (e.g., NaCl, KCl, and $FeCl_3$) in the hydrogel polymer network. However, it requires high concentrations of salt ions, thus limiting the biomedical applications of such gels owing to the fact that the normal ion concentration in the human physiological environment is less than 300 mM.[18,19] To address this issue, negatively charged micro/nanofibers have been proposed due to their ability to attract more cations in lower-concentration salt solutions and ensure relatively high conductivity.[20] Therefore, it is of great importance to enrich the good conductivity and sensing ability of ionic conductive hydrogels after immersion in low-concentration salt solutions.

Moreover, the fabrication of hydrogel-based functional devices with complex structures must meet different requirements. Conventional processing methods, such as precision machining, lithography, and thermal stretching, play an important role in the bioelectronics field.[21] However, these methods are not suitable for the processing of soft hydrogels with high water contents.[22] In this respect, three-dimensional (3D) printing technology presented by inkjet printing, flat printing, and direct writing printing provides a new strategy for the preparation of hydrogel-based electronic devices with high precision and complex structure.[23] These printing methods provide flexibility adjustment according to the characteristics of different materials, which is advantageous in the fabrication of hydrogel-based bioelectronic devices. Nevertheless, it still remains a great challenge to achieve critical feature combinations concerning high strength, stretchability, broad sensing range, and 3D printability for a new generation of electronic skins.

In this work, silk microfiber (SMF)/regenerated silk fibroin (RSF)/PAM triple-network composite hydrogels exhibiting excellent properties, such as stretchability, conductivity, strain-sensing ability, and 3D printability, were fabricated based on a simple white source curing method. The SF component and the cross-linked RSF hydrogel provide the advantages of good biocompatibility and biodegradability, which make SF one of the ideal natural materials for electronic skins.[24−26] The PAM hydrogel has been reported to have excellent stretchability and strain-sensing ability.[27] The addition of negatively charged SMF enhances the mechanical properties, conductivity, and sensing ability of hydrogels due to the interaction between SMF and RSF and the adsorption of cations. Moreover, the SMF, RSF, and PAM are expected to form a triple-network hydrogel structure under the effect of the initiator and cross-linker-based white light initiation, thus endowing the material with potential stretchability, conductivity, mechanical properties, strain-sensing ability, and 3D printability. The formation process and construction mechanism of the SMF/RSF/PAM triple-network hydrogel were explored. The morphology, structure, mechanical properties, strain/stress sensing properties, and conductive mechanism of the composite hydrogels were thoroughly analyzed. The 3D printability of the SMF/RSF/acrylamide (AM) ink and the strain-sensing ability of the 3D-printed composite hydrogel were verified. According to the results, it is evident that the SMF/RSF/PAM triple-network composite hydrogels hold significant promise for applications in skin tissue engineering.

https://doi.org/10.1021/acsbiomaterials.4c00201
ACS Biomater. Sci. Eng. 2024, 10, 3489−3499

MATERIALS AND METHODS

Preparation of Degummed Silk. The degummed silk was prepared by boiling the cocoon in a 0.5 wt % sodium carbonate solution for 30 min and then rinsing it with deionized water. The process was repeated twice, after which the degummed silk was dried and stored for further usage.

Preparation of RSF Solution. The degummed silk was dissolved in 9 M lithium bromide at 40 °C for 2 h, and the solution was then centrifuged at 3000 rpm for 10 min. After the 3 day dialysis in a semipermeable cellulose membrane (the molecular weight cutoff (MWCO) was 14,000 Da) to remove the ions, a 10 wt % RSF solution was obtained via water evaporation.

Preparation of SMF Suspension. A mixed solution based on 3 g of NaOH, 16 g of urea, and 81 g of H_2O was prepared and precooled to −12 °C according to the procedure reported in previous work.[28] The degummed silk (3 g) was dispersed into the precooled aqueous solution, followed by stirring for 10 min every 12 h. After 3 days, the mixture was dialyzed at 4 °C to remove the salt ions. The mixture was then sonicated at 300 W for 30 min. The SMF was harvested by centrifugation at 4500 rpm for 20 min and the removal of the supernatant. The 0.5 wt % SMF suspension was finally obtained by mixing SMF with water.

Preparation of Composite Hydrogels. The preparation process of the SMF/RSF/PAM composite hydrogel is shown in Figure 1a. The SMF suspension was sonicated at 300 W for 10 min and then mixed well with the mixture of AM (0.9 g) and RSF (20 wt %, 0.9 g). Deionized water was added to keep the volume of the mixture at ∼3 mL. After that, cross-linker *N*,*N*′-methylenebis(2-propenamide) (MBA) (10 mg/mL, 59 μL), initiator tris(2,2′-bipyridine)-dichlororuthenium(II) hexahydrate (Ru) (3.74 mg/mL, 90 μL), and ammonium persulfate (APS) (6.39 mg/mL, 90 μL) were thoroughly mixed with the above blend. The obtained solution was then transferred into different molds and exposed to a white light source (7 W) for 4 h to fabricate composite hydrogels. Slurries used for 3D printing and rheological testing were labeled as SMF/RSF/AM and SMF/RSF inks. Based on the mass ratio of SMF to the AM monomer (0.8, 1.6, 2.4, and 3.6%), the SMF/RSF/PAM hydrogels were labeled as SMF-0.8% (SMF-0.8%/RSF/PAM), SMF-1.6% (SMF-1.6%/RSF/PAM), SMF-2.4% (SMF-2.4%/RSF/PAM), and SMF-3.6% (SMF-3.6%/RSF/PAM), respectively. The RSF/PAM hydrogel was obtained by mixing AM and RSF. A PAM hydrogel was used as the control specimen.

Morphology and Size Characterization of SMFs. The SMF suspension (2 wt %) was dispersed on a silicon wafer and dried at room temperature. The SMF morphology was then observed by scanning electron microscopy (SEM) (S-4800, Hitachi, Japan) at 5 kV.

The SMF suspension (0.01 mg/mL) was dropped onto the carbon-film-coated copper grids and then characterized via transmission electron microscopy (TEM) (JEOL JEM-2100, Japan) at a voltage of 200 kV. The diameters of the nanofibrils were measured from the TEM images using Nano Measurer 1.2 software.

ζ-Potential Measurement of the SMF Suspension. The ζ-potential of the 2 wt % SMF suspension was measured using a Zetasizer instrument (Litesizer 500, Anton Paar, Austria).

Rheological Testing of Composite Inks. The SMF/RSF and SMF/RSF/AM inks were tested by means of an optical micro-rheometer (Rheolaser Master, Formulaction, France) at 25 °C for 40 min. The SLB represents the solid−liquid equilibrium values of slurries in the rheological test.

The rheological properties of composite inks were tested using a rotational rheometer (Haake RS150L Rheomete, Thermo Electron Co., Germany) with titanium alloy plates (a diameter of 20 mm and a gap of 0.3 mm) at 25 °C. The samples were brought to the equilibrium temperature for 1 min prior to the measurement. The shear viscosity was measured at shear rates ranging from 0.01 to 1000 s^{-1}. The frequency range was 0.1−100 Hz at a fixed strain of 1%, determined from the linear viscoelastic region. The oscillation logarithmic stress sweeps from 1 to 1000 Pa were conducted at a frequency of 1 Hz. The yield stress of samples was determined based on the crossover point where $G' = G''$.

Morphological and Structural Characterization of Hydrogels. The PAM, RSF/PAM, and SMF/RSF/PAM hydrogels were immersed in deionized water. The hydrogels were then subjected to liquid nitrogen conditions and freeze-drying. Finally, the samples were attached to the stage using a conductive adhesive and sputter-coated with platinum. Their morphology was observed by scanning electron microscopy (S-4800, Hitachi, Japan) at 5 kV.

Fourier Transform Infrared (FTIR) Spectroscopy Analysis of Samples. For FTIR measurements, the freeze-dried samples were tested using a Nicolet 8700 spectrometer equipped with attenuated total reflectance in the spectral region of 525−4000 cm^{-1} by accumulating 32 scans at a resolution of 4 cm^{-1}. PeakFit software was used to analyze the secondary structure of specimens.

Mechanical Property Measurements of Hydrogels. The mechanical properties of hydrogels were assessed using a mechanical testing machine (Instron 5969) at a temperature of 25 ± 2 °C and a relative humidity (RH) of 55 ± 5%. For the tensile tests, the 35 mm × 5 mm × 1 mm samples were fabricated using a silicone mold. After the mold was filled with the slurry, a white light source (7 W) was applied for 4 h. The tensile tests were performed at an extension rate of 50 mm/min. In the compression tests, the slurries were loaded into a syringe barrel with a diameter of 9 mm and exposed to white light for 4 h. The cylindrical hydrogels with 9 mm diameters and 7 mm heights were tested at a compression rate of 5 mm/min. The compressive strength of the hydrogel was set as the stress at a compressive strain of 90%. However, for the recycle loading−unloading compressive stress−strain test of the SMF/RSF/PAM hydrogel, the compressive strain was set as 60%.

Swelling Testing of Hydrogels. The PAM, RSF/PAM, and SMF/RSF/PAM hydrogels with diameters of 9 mm were immersed in deionized water for 24 h. The RSF/PAM and SMF-3.6%/RSF/PAM hydrogels were respectively immersed in phosphate-buffered saline (PBS) solution (pH 7.4, 10 mM) for 24 h to reach the swelling equilibrium point. A freeze-dried sample with a weight of m_0 was then obtained. The weights of the samples at the swelling equilibrium point were assumed to be m_1. The swelling ratio w was afterward calculated according to eq 1

$$w = \frac{m_1 - m_0}{m_0} \times 100\% \tag{1}$$

Strain-Sensing Performance of Hydrogels. The cylinder hydrogel with length l and radius r was immersed in a PBS solution for 24 h at room temperature. The immersed cylinder hydrogel was then connected between two parallel plate electrodes in a closed circuit. The current (I) was measured by means of a SourceMeter instrument (B2912A, Agilent) at voltage U = 1 V. The conductivity (σ) of hydrogel was calculated as follows[29]

$$\sigma = \frac{Il}{U \times \pi r^2} \tag{2}$$

The electrochemical workstation (PGSTAT204N, Metrohm, Switzerland) was afterward used to test the current in the stretching and compression process of the hydrogel at a voltage of 1 V. The corresponding resistance (R) was calculated according to Ohm's law as follows

$$R = \frac{U}{I} \tag{3}$$

The relative change rate of resistance was calculated according to the equation below

$$\frac{\Delta R}{R} = \frac{R - R_0}{R_0} \tag{4}$$

where R_0 and R are the resistances before and after strain/pressure exposure, respectively. The Gauge factor (GF) of the hydrogel was calculated as[9]

https://doi.org/10.1021/acsbiomaterials.4c00201
ACS Biomater. Sci. Eng. 2024, 10, 3489−3499

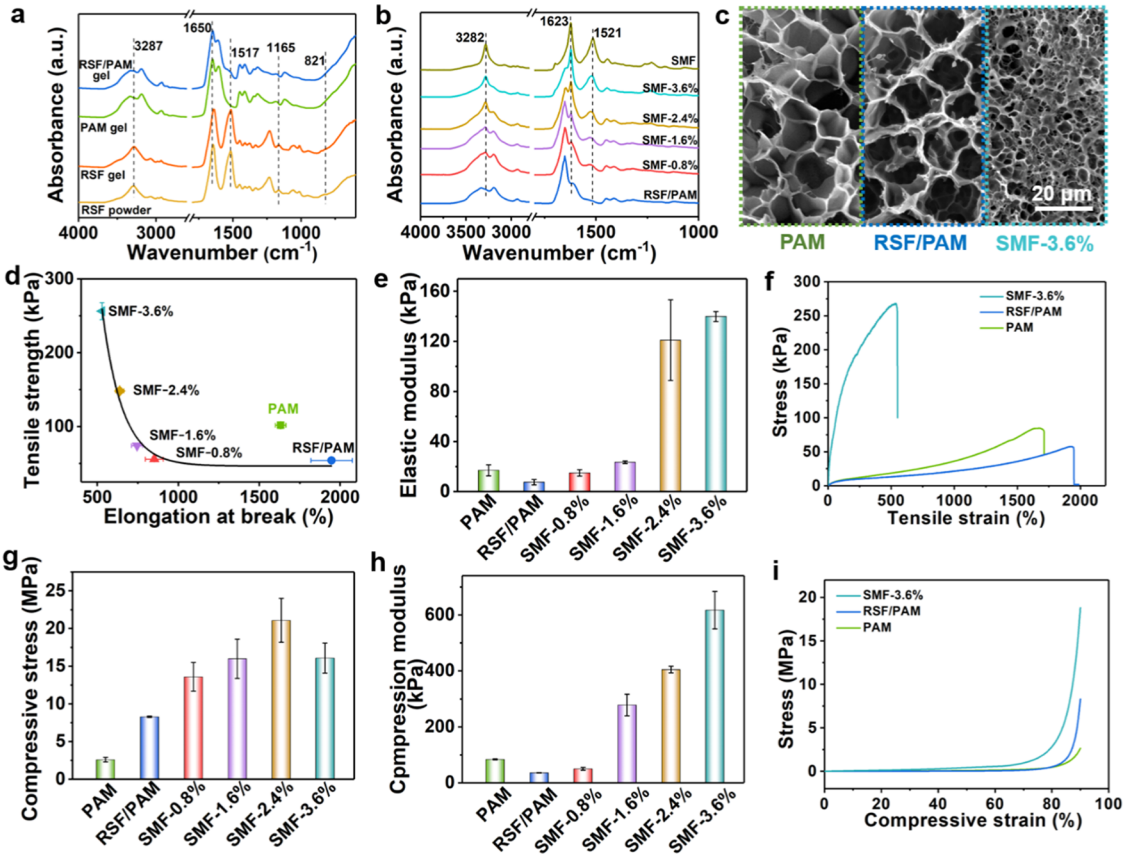

Figure 2. Secondary structure, morphology, and mechanical properties of composite hydrogels. (a) FTIR spectra of freeze-dried RSF powder, RSF hydrogel, PAM hydrogel, and RSF/PAM hydrogel. (b) FTIR spectra of freeze-dried SMF powder and SMF/RSF/PAM hydrogel. (c) SEM images of hydrogels. (d) Tensile strength and elongation at break, (e) elastic modulus, (f) tensile stress−strain curves, (g) compressive stress (90% strain), (h) compression modulus, and (i) compressive stress−strain curves of composite hydrogels.

$$GF = \frac{\Delta R/R}{\varepsilon} \quad (5)$$

where ε is the strain applied to the hydrogel.

3D Printing of Composite Inks. The SMF/RSF/AM ink was used for 3D printing, wherein the inner diameter and moving speed of the needle were 620 μm and 30 mm/s, respectively. The extrusion pressure was 32−35 kPa. The line spacing was 2 mm, and the angle between the two lines was 90°. Prior to the printing, 0.9 g of AM was dissolved in 1 mL of SMF (2 wt %) suspension, followed by the addition of 0.28 g of freeze-dried RSF powder. Then, 200 μL of Ru (3.74 mg/mL), 200 μL of APS (6.39 mg/mL), and 120 μL of MBA (10 mg/mL) solutions were added to the mixture. Once the SMF/RSF/AM/oxidized bacterial cellulose (OBC) ink was prepared, 4 g of OBC (6 wt %) was added, and the blend was exposed to stirring. The 2,2,6,6-tetramethylpiperidine-1-oxyl (TEMPO)-mediated OBC could further improve the printing precision. The hexagonal circular cylinder model was designed by means of 3D builder software. The model was then imported into GeSim software to print 3D scaffolds. The white light was used to cure the scaffolds for 4 h after printing. The printed hydrogel samples were immersed in PBS solution for 24 h for further sensing performance tests.

RESULTS AND DISCUSSION

Fabrication Mechanism of SMF/RSF/PAM Triple-Network Composite Hydrogels. Based on the design mechanism of triple-network composite hydrogels, white light was used to cure the SMF/RSF/PAM hydrogel. RSF cross-linking and AM monomer polymerization occurred simultaneously in the Ru/APS system. Meanwhile, another network was formed based on SMF and RSF. Thus, SMF/RSF/PAM triple-network hydrogels were prepared via a simple, fast, and mild one-step photocuring method (Figure 1a).

The first network was the weak physical network between SMF and RSF due to the electrostatic interaction between the negative charges of SMF and the positive charges of RSF (Figure 1b). Figure 1c shows the microfiber morphology of the SMF with a diameter of ∼7 μm (Figure S1), and its aspect ratio was more than 100. The sodium hydroxide/urea system broke the hydrogen bonds between the molecular chains of the degummed silk to obtain SMFs. The SMFs still retained a highly crystalline structure after alkaline treatment, and the β-sheet content was as high as 33.5%.[28] Therefore, the microfiber could be used as the reinforcement filler to prepare composite hydrogels with improved stiffness and creep resistance. In addition, the SMF can also be used to enhance the printability of the hydrogel and the fidelity of the printing scaffold.[30,31] As shown in Figure 1d, the ζ-potential values of the RSF solution (pH 6.33) and SMF suspension (pH 7.30) are 0.7 and −21.4 mV, respectively, indicating that weak electrostatic interaction may exist between the RSF and SMF. The reason why the SMF is negatively charged is that the amorphous structure of the degummed silk is more likely to be destroyed by the oxhydryl group, forming the carboxyl group on the surface.[32,33] The negative charges on the surface of the SMF attract the positive charges in RSF with amphoteric charges to form a weak physical network gel. In addition, SMFs can combine with cations to promote the migration of cations in the

https://doi.org/10.1021/acsbiomaterials.4c00201
ACS Biomater. Sci. Eng. 2024, 10, 3489−3499

hydrogel[20] and improve the ionic conductivity of the hydrogel. After mixing the RSF (20 wt %) and SMF (2 wt %) solutions, the mixture exhibited the gel state due to the formation of a physical network in the hydrogel caused by the electrostatic force between the SMF and RSF.

The second element of the hydrogel was the cross-linked RSF network (Figure 1f). Figure 1g depicts the reaction mechanism of the cross-linked RSF network under the white light source and Ru. Herein, Ru compounds absorb white light to form excited-state metal ligands, and APS acts as an electron acceptor. The cross-linked reaction occurred between the tyrosine side chains of RSF to form dityrosine. The third component was the cross-linked PAM network (Figure 1h). Figure 1i shows the cross-linking mechanism of the PAM network. The AM monomer was polymerized under the effect of photosensitizer Ru and the white light source, and it was also cross-linked by MBA.[27,34,35] The formation time of the RSF/PAM hydrogel was short (less than 2 min) under white light illumination (Figure S3). Figure 1g,i depicts the composite hydrogel formed by the photo-cross-linking of RSF and the polymerization of PAM. Since Ru did not combine with the polymer, it could be separated through soaking.

The optical microrheology testing revealed that the RSF or RSF/AM solution formed a hydrogel after being mixed with the SMF for 10 min (Figure S4). Moreover, the addition of AM decreased the elasticity of the composite hydrogel due to the loose structure of PAM. Once the RSF or RSF/AM solution was mixed with the SMF suspension, both compounds changed their states from liquid, with a solid−liquid balance (SLB) above 0.5, to solid, with an SLB below 0.5 (Figure S4b). Therefore, the formation of a weakly cross-linked hydrogel is of great significance for the enhancement of ink fidelity in 3D printing. The SMF/RSF/PAM hydrogel presented stretchability, conductivity, strain-sensing ability, and 3D printability (Figure 1j).

Structure, Morphology, and Mechanical Properties of Composite Hydrogels. The structure and morphology of composite hydrogels influence their mechanical properties, ion transport performance, and strain-sensing ability. Figure 2a,b shows the FTIR spectra of the freeze-dried RSF hydrogel, PAM hydrogel, RSF/PAM hydrogel, and RSF powder. The peak of the RSF powder near 821 cm^{-1} represents the characteristic vibration of benzene with a pair substitution on the side chain of tyrosine. However, this peak was absent in the spectra of RSF and RSF/PAM hydrogels, indicating that the tyrosine in RSF was cross-linked. In addition, the characteristic peaks of RSF and PAM/RSF hydrogels near 1165 cm^{-1} weakened compared with that of RSF powder, representing the reduction of tyrosine side chains.[36] For amide I, peaks at 1697 and 1623 cm^{-1} belonged to the β-sheet and peaks at 1650 and 1678 cm^{-1} were due to random coil/helix and β-turn, respectively. In Figure 2a, peaks can be observed at 1645 cm^{-1} for RSF powder and 1638 cm^{-1} for the RSF hydrogel. The conformation contents of the samples were calculated from the deconvolution of amide I peaks (Table S1). The β-sheet content of the cross-linked RSF hydrogel was 11.1%, which is slightly higher than that of RSF powder. Therefore, the photo-cross-linked RSF hydrogel mainly consisted of random coil/helix conformations and had low crystallinity.[37] The absorbance peak at 3287 cm^{-1} could be assigned to an amino. Due to the formation of multiple hydrogen bonds within the inter/intrachains, broader peaks could be observed at 3287 cm^{-1} in PAM and RSF/PAM hydrogels compared to those on the RSF hydrogel. With the increase in SMF content in SMF/RSF/PAM hydrogels, the typical peaks at 1623 and 1521 cm^{-1} increased (Figure 2b). The peak at 3279 cm^{-1} represents hydrogen-bonded NH stretching.[38] The peaks of the SMF/RSF/PAM hydrogels at 3282 cm^{-1} became narrowed with increasing SMF content. The narrowed peak indicates a weakened hydrogen-bonding interaction.[39] The aggregated RSF and SMF may cause the number of hydrogen bonds to be reduced in SMF/RSF/PAM hydrogels. Therefore, the cross-linked PAM, RSF/PAM, and SMF/RSF/PAM hydrogels contained single, double, and triple networks (Figure S5), respectively, under the effect of the Ru/APS system and white light radiation.

Figure 2c depicts the cross-sectional morphology of freeze-dried PAM, RSF/PAM, and SMF/RSF/PAM hydrogels. Thanks to the uniformly distributed molecular chains, all of these hydrogels exhibited a uniform pore structure. The pore sizes in PAM, RSF/PAM, and SMF/RSF/PAM hydrogels were 14.4 ± 1.4, 15.3 ± 1.9, and 4.3 ± 1.1 μm, respectively. Although PAM and RSF/PAM hydrogels had similar pore sizes, the pores in the former were completed and closed, while those in the RSF/PAM hydrogel were interconnected. Compared with PAM and RSF/PAM hydrogels, the SMF/RSF/PAM hydrogel showed a dense structure with interconnected pores. The SMF and RSF gels caused physical cross-linking in the PAM hydrogel network. The abundant networks and relatively dense pore structure endowed the SMF/RSF/PAM hydrogel with good mechanical properties and a broad strain-sensing range.

The excellent mechanical properties of hydrogel materials are the basis for strain sensors. Figure 2d shows the influence of SMF on the stress−strain properties of composite hydrogels. Figure 2e displays the elastic moduli of the composite hydrogels. The tensile strength and modulus of RSF/PAM hydrogels decreased slightly compared with those of PAM hydrogels, while the elongation at break of RSF/PAM hydrogels increased. The RSF network increased the molecular chain spacing of PAM and decreased the cross-linking density of the PAM hydrogel network, thus increasing the degree of PAM molecular chain slip. With the increase of SMF content, the tensile stress and elastic modulus increased, and the elongation at break decreased. According to the stress−strain curves (Figure 2f), the toughnesses of PAM, RSF/PAM, and SMF-3.6%/RSF/PAM hydrogels were 0.62, 0.48, and 1.06 MJ/m^3, respectively. The addition of SMF effectively increased the toughness of composite hydrogels due to its high β-sheet structure.

The compressive stress (90% strain) and compression modulus (5−10% strain) of the hydrogel samples are shown in Figure 2g,h. The compressive strength of the RSF/PAM hydrogel at 90% compressive strain was greater than that of the PAM hydrogel (Figure 2g) due to the RSF network in the former hydrogel, which increases the rigidity. With a further increase in the SMF content of SMF/RSF/PAM hydrogels, the compressive stress and compression modulus of the composite hydrogels increased due to the high β-sheet crystalline structure of SMF[28] and the rigid structure of SMF and RSF aggregates in the PAM network. The rigid structure increased the strength and modulus and prevented the slip of molecular chains in the PAM network. When the compressive strain was lower than 80%, SMF-2.4% and SMF-3.6% hydrogels showed similar compressive strength (Figure S6). However, the

https://doi.org/10.1021/acsbiomaterials.4c00201
ACS Biomater. Sci. Eng. 2024, 10, 3489−3499

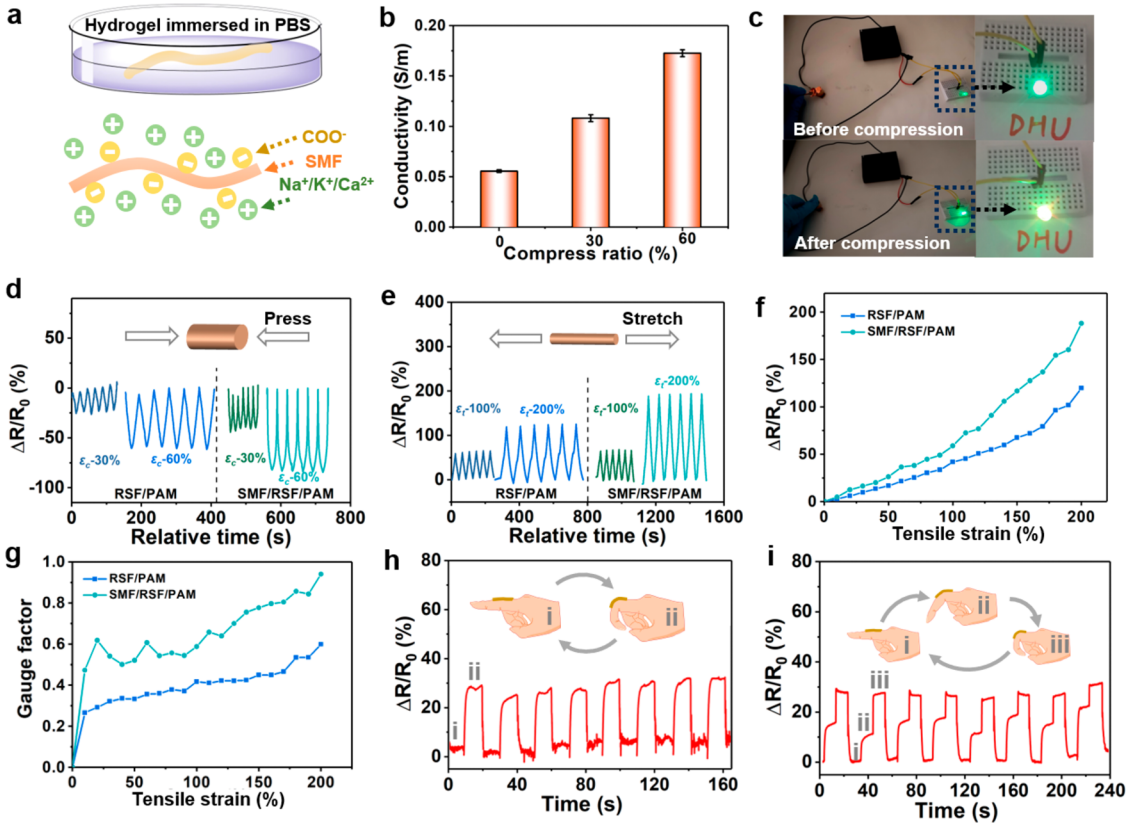

Figure 3. Conductivity and strain-sensing ability of composite hydrogels. (a) Hydrogel is immersed in PBS (10 mM), and the $Na^+/K^+/Ca^{2+}$ ions are attracted by SMF. (b) Conductivity of the SMF/RSF/PAM hydrogel-based strain sensor with different compression ratios. (c) Photographs of the LED light before and after compression. Strain sensors of hydrogels under (d) compression (ε_c = 30 and 60%) and (e) tensile (ε_t = 100 and 200%) loading. (f) Relative resistance changes and (g) gauge factor variations of the composite hydrogel-based sensors under the applied tension. Relative resistance changes upon (h) two and (i) three movements of the strain sensor on the fingers. The SMF-to-AM mass ratio in the SMF/RSF/PAM hydrogel was 3.6%.

compressive strength of SMF-3.6% was lower than that of SMF-2.4% when the compressive strain was 90%. The stress concentration may start to emerge in the SMF-3.6% hydrogel due to the dual function of relatively high addition content of SMF and large compressive strain.[40] Figure 2i depicts the compressive stress−strain curves of composite hydrogels. Compared with RSF/PAM and PAM hydrogels, the SMF/RSF/PAM hydrogel with a 3.6% SMF content underwent obvious stress changes under the same compressive strain. The elasticity and recovery of the SMF/RSF/PAM hydrogel were tested by continuously applying compression−relaxation cycles (Figure S7). After a relatively large hysteresis loop in the first loading−unloading cycle, the compression stress−strain curve for the rest of the cycles exhibited relatively small hysteresis loops and the corresponding loops were highly consistent with each other (Figure S7a). A slight decrease in the recovery percentage of 94.7% was observed for the first cycle with a compressive strain of 60% (Figure S7b). After that, the recovery percentage remained constant for the second to tenth cycles. Thus, given the excellent mechanical properties, the SMF/RSF/PAM hydrogel with 3.6% SMF content was chosen for further analysis of the conductivity and strain-sensing ability.

Conductivity and Strain-Sensing Ability of the SMF/RSF/PAM Hydrogel. The fluid environment of the human body, containing Ca^{2+}, Cl^-, Na^+, and PO_4^{3-} ions, has electrical conductivity. Therefore, the hydrogels are usually formed in the electrolyte buffer salt solution, such as PBS, for biomedical (especially tissue engineering) applications.[41] The swelling of composite hydrogels immersed in deionized water and PBS (10 mM) was further explored in this study. With the increase of SMF content, the swelling property of the hydrogel decreased after immersion in deionized water (Figure S8a). Compared with that of the RSF/PAM hydrogel, the swelling ratio of the SMF-3.6%/RSF/PAM hydrogel decreased by more than 60% (Figure S8b). The dense structure of the internal network of the SMF/RSF/PAM hydrogel restricted the movement of molecular chains. The RSF/PAM and SMF/RSF/PAM hydrogels were immersed in PBS (including Na^+, K^+, Cl^-, and PO_4^{3-}) to achieve swelling equilibrium and obtain electrical conductivity (Figure 3a). The swelling properties of the hydrogels in PBS are shown in Figure S9. The results revealed that the swelling performance of the RSF/PAM and SMF/RSF/PAM hydrogels in PBS was the same as that in deionized water. Figure S9b,c displays the cross-sectional images of a freeze-dried swelling hydrogel in PBS. The red arrows represent the phosphate particles adsorbed in the hydrogel. The PBS solution was uniformly distributed in the hydrogel network after swelling, and the movement of these salt ions in the hydrogel is a necessary condition for electric conduction.[42] The conductivity of the SMF/RSF/PAM hydrogel after immersion in PBS (10 mM) was afterward analyzed. The conductivity was enhanced with the increasing compression ratio (Figure 3b). The pressure applied to the

https://doi.org/10.1021/acsbiomaterials.4c00201
ACS Biomater. Sci. Eng. 2024, 10, 3489−3499

Table 1. Comparison of SMF/RSF/PAM Hydrogels with Other Ion-Conducting Hydrogels[a]

sample	electrolyte solution	concentration of salt ions		conductivity (S/m)	sensing sensitivity (GF)	refs
SA/PAM	NaCl	>300 mM	4.43 wt %	0.056	0−2.0 (0−200%) 2.0−2.7 (200−1800%)	9
HPC/PVA	NaCl	>300 mM	5 M	3.4	0.984 (0−400%)	45
PA	$FeCl_3$	>300 mM	2 M	15	2.02 (0−200%)	46
CNF/PAM	KCl	<300 mM	100 mM	0.05		20
RSF/PAM/OBC	PBS	<300 mM	10 mM		0.68−1.14 (0−80%)	14
CNC/PVA/PVP	Fe^{3+}	<300 mM	1.8 mM		0.478 (0−200%)	47
PVA/PSBMA		<300 mM		0.051	0.8−1.5 (0−50%) 1.5 (50−300%)	48
RSF/PAM	PBS	<300 mM	10 mM	0.16	0.6 (0−200%)	this work
SMF/RSF/PAM	PBS	<300 mM	10 mM	0.056	0.9 (0−200%)	this work

[a]SA, sodium alginate; HPC, hydroxypropyl cellulose; PVA, poly(vinyl alcohol); PA, polyampholyte; CNF, cellulose nanofibers; CNC, cellulose nanocrystal; PVP, poly(vinylpyrrolidone); PSBMA, poly[2(methacryloyloxy)ethyl]dimethyl-(3-sulfopropyl); PA, polyampholyte.

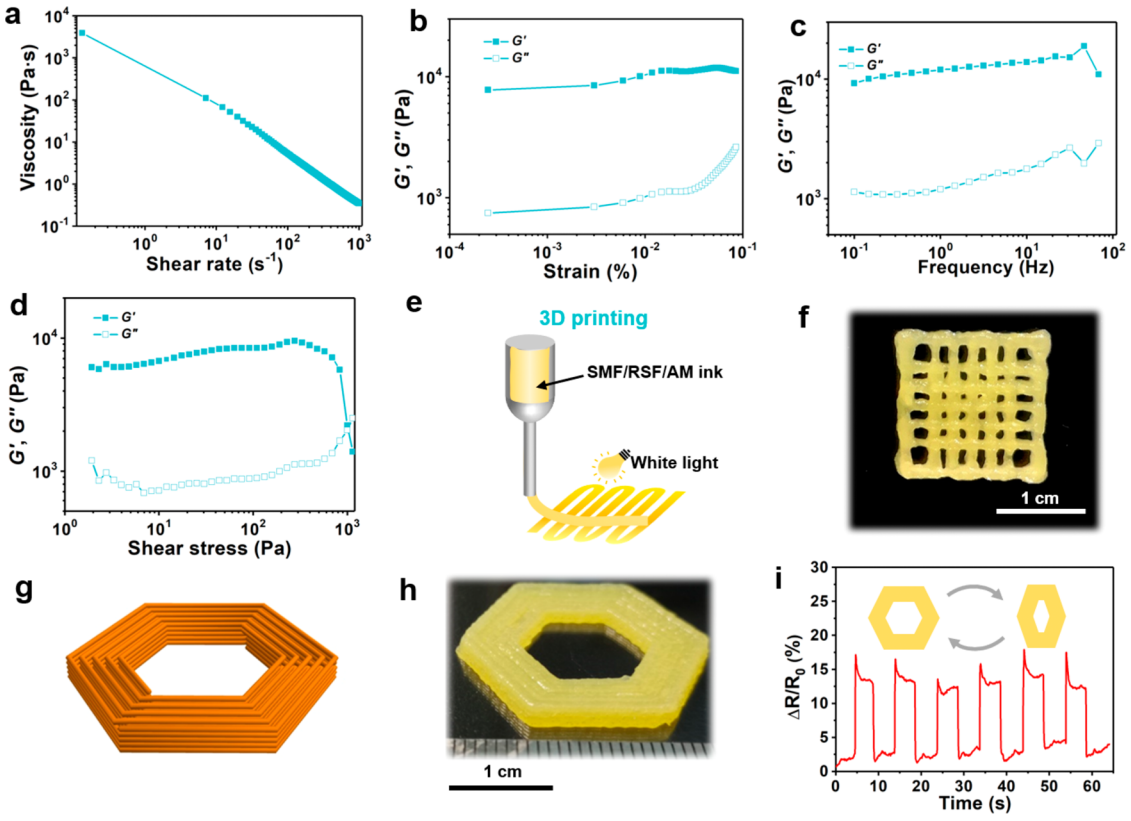

Figure 4. Rheological data and 3D printability of the SMF/RSF/AM ink. (a) Steady-shear behavior. (b) Storage modulus (G') and loss modulus (G'') as a function of strain. (c) G' and G'' as a function of frequency. (d) Oscillatory rheological behavior. (e) Schematic image of 3D printing. (f) Optical image of the mesh pattern printed by SMF/RSF/AM ink. (g) Image of the hexagonal circular cylinder with five layers in the printer. (h) 3D view of the hexagonal circular cylinder with multilayers printed using the SMF/RSF/AM/OBC ink. (i) Relative resistance changes of the printed composite hydrogel sensor with respect to cyclic shape variations. The SMF-to-AM mass ratio in the SMF/RSF/PAM hydrogel was 3.6%.

hydrogel enhanced the ion concentration and promoted the flow of cations and anions,[43] further increasing the conductivity. Figure 3c depicts the brightness change of the LED light before and after compression of the hydrogel. Once the compression strain increased, the light became brighter, illustrating the increase in conductivity.

The relative change rates of the resistance in RSF/PAM hydrogels and SMF/RSF/PAM hydrogel-based strain sensors were tested under cyclic loading by applying different compression ratios (ε_c = 30 and 60%) and stretch ratios (ε_t = 100 and 200%). The resistance change rates both increased with the increase in compressive/tensile strain (Figure 3d,e). The resistance decreased when the hydrogel was compressed, while it increased upon stretching the hydrogel. Previous literature[44] reported that the pressure sensor sensitivity (S) was defined as the curve slope of the resistance rate changing with pressure. Also, the pressure sensor sensitivity of the hydrogel consists of multiple regions. The pressure sensor sensitivity of composite hydrogels is shown in Figure S10. When the pressure was less than 1.5 kPa or higher than 4.5 kPa, the pressure sensor sensitivity of the RSF/PAM hydrogel was 0.2 or 0.026 kPa^{-1}, respectively, indicating that the pressure sensor sensitivity decreased with the increase of pressure. The SMF/RSF/PAM hydrogel exhibited a similar changing trend of pressure sensor sensitivity to the RSF/PAM hydrogel. When the pressure of the SMF/RSF/PAM hydrogel was less than 7.5 kPa^{-1} or higher than 50.0 kPa^{-1}, the pressure sensor sensitivity was 0.014 kPa^{-1} or 4.5 × 10^{-5} kPa^{-1},

https://doi.org/10.1021/acsbiomaterials.4c00201
ACS Biomater. Sci. Eng. 2024, 10, 3489−3499

respectively. Therefore, the addition of SMF increased the applicable pressure range. With the change of tensile strain, the curve slope of the SMF/RSF/PAM hydrogel was obviously higher than that of the RSF/PAM hydrogel, illustrating the better sensitivity of the former hydrogel (Figure 3f). Moreover, the sensing sensitivity (GF) of the SMF/RSF/PAM hydrogel was greater than that of the RSF/PAM hydrogel under the same tensile strain (Figure 3g and Table 1). This indicated that the addition of SMF increased the strain-sensing properties of the composite hydrogel. The SMF/RSF/PAM hydrogel presented a wide strain detection range of 0−200%, and its sensing sensitivity reached 0.95. The RSF with amphoteric charges attracted the positive and negative ions in the PBS. The negative charge of SMF in the composite hydrogel assembled cations (such as Na^+, K^+, and Ca^{2+}) from PBS on its surface (Figure 3a), resulting in an increase in ion conductivity and sensor sensitivity. Therefore, the composite hydrogel exhibited high conductivity after being immersed in a 10 mM PBS solution.

To evaluate the SMF/RSF/PAM gel-based ionic skin in a real work environment, the hydrogel was used as the strain sensor to detect finger movement. The ionic skin can sense finger deformation, which influences the resistance of the hydrogel. In this work, the ionic skin was stretched from its original state with the joint flexed from a straight state to a bent state, inducing the resistance change ($\Delta R/R_0$) of the ionic skin (Figure 3h). Once the finger returned back to the straight state, the resistance also returned to its initial state quickly. The different deformations induced by finger bending caused the resistance of the ionic skin to increase to various levels (Figure 3i). The SMF/RSF/PAM gel-based ionic skin can not only clearly monitor the joint flexing but also distinguish between the bending angles reflexed by the resistance change amplitude. The variation in resistance was completely synchronized with the joint flexing repetition without any hysteresis.

A comparison of SMF/RSF/PAM hydrogels with other ion-conducting composite hydrogels is presented in Table 1. In order to improve the conductivity and sensing sensitivity of the hydrogels, high concentrations of salt ions (>300 mM) were usually applied to immerse the composite hydrogels. According to the literature, the highest conductivity and GF of composite ion-conducting hydrogels could reach 15 and 2.7 S/m, respectivity.[9,46] However, the high concentration of salt ions limits the in vivo applications because the normal ion concentration in the human physiological environment is less than 300 mM.[18,19] Compared with other hydrogels with low concentrations of salt ions (<300 mM),[14,20,47] the composite hydrogels fabricated in this work exhibited higher conductivity. The GF of the SMF/RSF/PAM hydrogel after immersion in a low-concentration (10 mM) salt solution was similar to that of HPC/PVA hydrogel and higher than that of CNC/PVA/PVA hydrogel. Moreover, it reached the strain range of the PVA/PSBMA hydrogel. Furthermore, the SMF/RSF/PAM hydrogels may have wide applications in wearable and implantable electronic fields due to the abundant source and excellent comprehensive properties (e.g., good biocompatibility, biodegradability, and harmless degradable products) of SF.[49,50] Therefore, this hydrogel not only exhibited similar mechanical properties but also identical ion concentrations with biological tissues, having great application potential in biomaterial fields.

3D Printability of SMF/RSF/AM Inks. The printability of the SMF-3.6%/RSF/AM gel ink was demonstrated by using a rotational rheometer. The SMF/RSF/AM gel ink showed shear thinning characteristics before photocuring (Figure 4a), which was necessary for extrusion printing. When the strain was less than 1%, the values of storage modulus (G') and loss modulus (G'') remained unchanged (Figure 4b), which could be regarded as linear viscoelasticity (LVE).[51] The relationship between G', G'', and the shear frequency in the LVE region is shown in Figure 4c. Since G' was higher than G'' in the frequency range of 10^{-1}−10^{2} Hz, the ink was concluded to be in the elastic solid state. Moreover, G' was an order of magnitude higher than G'', indicating that the ink could well maintain the printing shape. Moreover, G' was higher than G'' at low shear stress. Once the G' value approached G'', the corresponding stress value of 1000 Pa was inferred to be the yield stress of the ink (Figure 4d). The ink showed a viscoelastic solid state when the shear stress was lower than the yield stress. Besides, the ink was in a viscoelastic fluid state when the shear stress was greater than the yield stress. In order to maintain the stability and fidelity of the printing shape, the knowledge of the solid-state behavior of the ink is essential for 3D printing with non-in-situ cross-linking extrusion.[52] The rheological test results indicated that the SMF/RSF/AM ink met the requirements for 3D printing.

Figure 4e depicts the schematic diagram of 3D printing using the SMF/RSF/AM ink under a white light source. The SMF/RSF/AM ink can form uniform lines at the outlet of the printing needle. The 3D-printed hydrogel scaffold had a grid structure, and the lines merged well with each other (Figure 4f). The printing precision of the SMF/RSF/AM ink could be improved by adding 4 g of OBC nanofibers (6 wt %). According to the designed hexagonal circular cylinder model (Figure 4g), a hexagonal circular cylinder was printed using the composite ink. The printing ink could completely copy the line path designed by the software, which indicated high printing precision (Figure 4h). In particular, the three-dimensional structure of the hexagonal ring cylinder with multilayers was printed by this ink. As shown in Figure 4i, the 3D-printed composite hydrogel scaffold presented a strain-sensing performance.

CONCLUSIONS

In summary, a simple and convenient method to prepare SMF/RSF/PAM hydrogels with stretchability, conductivity, strain-sensing ability, and 3D printability for a dual-signal response of electronic skins was proposed. The composite hydrogel had a triple-network structure: multiple weakly cross-linked SMF/RSF networks, covalently bonded RSF networks, and covalently bonded PAM networks. The mechanical properties of the SMF/RSF/PAM hydrogel exceeded those of the RSF/PAM hydrogel due to the addition of SMF, inducing the formation of new cross-linking networks. The tensile strength, compressive stress, and compressive modulus of the SMF/RSF/PAM composite hydrogel were as high as 256.5 ± 11.5 kPa, 16.1 ± 2.0 MPa, and 617.4 ± 67.1 kPa, respectively. The SMF/RSF/PAM hydrogel retained its conductivity and strain-sensing ability after immersion in PBS due to the absorption effect of negative charges from SMF on cations in PBS. Moreover, the contact and separation of SMF contributed to the increase of sensitivity of the SMF/RSF/PAM hydrogel during the cyclic loading process. The SMF/RSF/PAM hydrogel can be used for monitoring the joint movements and related motion amplitudes. 3D printability enables the composite hydrogel to meet the requirements for facilitating personalized customization. The ionic hydrogel-

https://doi.org/10.1021/acsbiomaterials.4c00201
ACS Biomater. Sci. Eng. 2024, 10, 3489−3499

based strain sensors have great application potential in skin tissue engineering.

■ ASSOCIATED CONTENT

Supporting Information

The Supporting Information is available free of charge at https://pubs.acs.org/doi/10.1021/acsbiomaterials.4c00201.

Relative scale of SMF (Figure S1); physical gelation process of the RSF/SMF hydrogel (Figure S2); gelation process of the RSF/PAM hydrogel under white light (Figure S3); gelation time and phase transition of SMF/RSF and SMF/RSF/AM inks (Figure S4); schematic images of composite hydrogels with different networks (Figure S5); compressive strengths of SMF-2.4% and SMF-3.6% at different compressive strains (Figure S6); recycle loading−unloading compressive stress−strain curves and recovery percentages of composite hydrogels (Figure S7); swelling of composite hydrogels in deionized water and PBS (Figures S8 and S9); relative resistance changes of composite hydrogel sensors on applied tension (Figure S10); and secondary structures of RSF powder and RSF gel (Table S1) (PDF)

■ AUTHOR INFORMATION

Corresponding Author

Yaopeng Zhang − *State Key Laboratory for Modification of Chemical Fibers and Polymer Materials, College of Materials Science and Engineering, Donghua University, Shanghai 201620, China;* orcid.org/0000-0002-7175-6150; Email: zyp@dhu.edu.cn

Authors

Qianqian Niu − *State Key Laboratory for Modification of Chemical Fibers and Polymer Materials, College of Materials Science and Engineering, Donghua University, Shanghai 201620, China*

Li Huang − *State Key Laboratory for Modification of Chemical Fibers and Polymer Materials, College of Materials Science and Engineering, Donghua University, Shanghai 201620, China*

Suna Fan − *State Key Laboratory for Modification of Chemical Fibers and Polymer Materials, College of Materials Science and Engineering, Donghua University, Shanghai 201620, China;* orcid.org/0000-0001-6508-360X

Xiang Yao − *State Key Laboratory for Modification of Chemical Fibers and Polymer Materials, College of Materials Science and Engineering, Donghua University, Shanghai 201620, China*

Complete contact information is available at: https://pubs.acs.org/10.1021/acsbiomaterials.4c00201

Author Contributions

Y.Z. conceived and directed this research. Q.N. performed the experiments, analyzed the data, and wrote the manuscript. L.H. designed and performed the experiments. S.F. and X.Y. directed the strain-sensing measurement of composite hydrogels. All authors contributed to the preparation of the manuscript.

Notes

The authors declare no competing financial interest.

■ ACKNOWLEDGMENTS

This work was sponsored by the National Natural Science Foundation of China (52173031, 52273125), the Basic Research Project of the Science and Technology Commission of Shanghai Municipality (21JC1400100), the Fundamental Research Funds for the Central Universities (2232019A3-06), the China Postdoctoral Science Foundation (2022M720708), and the Oriental Talent Plan (Leading Talent Program, No. 152).

■ ABBREVIATIONS

SMF, silk microfiber; RSF, regenerated silk fibroin; PAM, polyacrylamide; SF, silk fibroin; AM, acrylamide; MBA, *N*,*N*′-methylenebis(2-propenamide); Ru, tri(2,2′-bipyridine)-dichlororuthenium(II) hexahydrate; APS, ammonium persulfate; SEM, scanning electron microscopy; TEM, transmission electron microscopy; FTIR, Fourier transform infrared; PBS, phosphate-buffered saline; GF, gauge factor; OBC, oxidized bacterial cellulose; TEMPO, 2,2,6,6-tetramethylpiperidine-1-oxyl; SLB, solid−liquid balance; LVE, linear viscoelasticity; SA, sodium alginate; HPC, hydroxypropyl cellulose; PVA, poly(vinyl alcohol); PA, polyampholyte; CNF, cellulose nanofiber; CNC, cellulose nanocrystal; PVP, poly(vinylpyrrolidone); PSBMA, poly[2(methacryloyloxy)ethyl]dimethyl-(3-sulfopropyl)

■ REFERENCES

(1) Zhang, H.; Guo, J.; Wang, Y.; Sun, L.; Zhao, Y. Stretchable and Conductive Composite Structural Color Hydrogel Films as Bionic Electronic Skins. *Adv. Sci.* **2021**, *8*, No. 2102156.

(2) Zhang, M.; Gong, S.; Hakobyan, K.; Gao, Z.; Shao, Z.; Peng, S.; Wu, S.; Hao, X.; Jiang, Z.; Wong, E. H.; Liang, K.; Wang, C. H.; Cheng, W.; Xu, J. Biomimetic Electronic Skin through Hierarchical Polymer Structural Design. *Adv. Sci.* **2023**, *11*, No. 2309006, DOI: 10.1002/advs.202309006.

(3) Lim, H. R.; Kim, H. S.; Qazi, R.; Kwon, Y. T.; Jeong, J. W.; Yeo, W. H. Advanced Soft Materials, Sensor Integrations, and Applications of Wearable Flexible Hybrid Electronics in Healthcare, Energy, and Environment. *Adv. Mater.* **2019**, *32*, No. 1901924, DOI: 10.1002/adma.201901924.

(4) Davidson-Rozenfeld, G.; Chen, X.; Qin, Y.; Ouyang, Y.; Sohn, Y. S.; Li, Z.; Nechushtai, R.; Willner, I. Stiffness-Switchable, Biocatalytic pH-Responsive DNA-Functionalized Polyacrylamide Cryogels and Their Mechanical Applications. *Adv. Funct. Mater.* **2023**, *34*, No. 2306586, DOI: 10.1002/adfm.202306586.

(5) Wang, L.; Duan, L.; Liu, G.; Sun, J.; Shahbazi, M. A.; Kundu, S. C.; Reis, R. L.; Xiao, B.; Yang, X. Bioinspired Polyacrylic Acid-Based Dressing: Wet Adhesive, Self-Healing, and Multi-Biofunctional Coacervate Hydrogel Accelerates Wound Healing. *Adv. Sci.* **2023**, *10*, No. 2207352.

(6) Lee, Y. W.; Kim, J. K.; Bozuyuk, U.; Dogan, N. O.; Khan, M. T. A.; Shiva, A.; Wild, A. M.; Sitti, M. Multifunctional 3D-Printed Pollen Grain-Inspired Hydrogel Microrobots for on-Demand Anchoring and Cargo Delivery. *Adv. Mater.* **2023**, *35*, No. 2209812.

(7) Liu, S.; Li, L. Ultrastretchable and Self-Healing Double-Network Hydrogel for 3D Printing and Strain Sensor. *ACS Appl. Mater. Interfaces* **2017**, *9*, 26429−26437.

(8) Chen, F.; Lu, S.; Zhu, L.; Tang, Z.; Wang, Q.; Qin, G.; Yang, J.; Sun, G.; Zhang, Q.; Chen, Q. Conductive Regenerated Silk-Fibroin-Based Hydrogels with Integrated High Mechanical Performances. *J. Mater. Chem. B* **2019**, *7*, 1708−1715.

(9) Zhang, X.; Sheng, N.; Wang, L.; Tan, Y.; Liu, C.; Xia, Y.; Nie, Z.; Sui, K. Supramolecular Nanofibrillar Hydrogels as Highly Stretchable, Elastic and Sensitive Ionic Sensors. *Mater. Horiz.* **2019**, *6*, 326−333.

(10) Niu, Q.; Wei, H.; Hsiao, B. S.; Zhang, Y. Biodegradable Silk Fibroin-Based Bio-Piezoelectric/Triboelectric Nanogenerators as Self-Powered Electronic Devices. *Nano Energy* **2022**, *96*, No. 107101.
(11) Wang, Q.; Ling, S.; Liang, X.; Wang, H.; Lu, H.; Zhang, Y. Self-Healable Multifunctional Electronic Tattoos Based on Silk and Graphene. *Adv. Funct. Mater.* **2019**, *29*, No. 1808695.
(12) Niu, Q.; Huang, L.; Lv, S.; Shao, H.; Fan, S.; Zhang, Y. Pulse-Driven Bio-Triboelectric Nanogenerator Based on Silk Nanoribbons. *Nano Energy* **2020**, *74*, No. 104837.
(13) Zhang, Y.; Lu, H.; Zhang, M.; Hou, Z.; Li, S.; Wang, H.; Wu, X. E.; Zhang, Y. In Situ Mineralizing Spinning of Strong and Tough Silk Fibers for Optical Waveguides. *ACS Nano* **2023**, *17*, 5905−5912.
(14) Geng, Y.; Liu, T.; Zhao, M.; Wei, H.; Yao, X.; Zhang, Y. Silk Fibroin/Polyacrylamide-Based Tough 3D Printing Scaffold with Strain Sensing Ability and Chondrogenic Activity. *Composites, Part B* **2024**, *271*, No. 111173.
(15) Ge, D.; Mi, Q.; Gong, R.; Li, S.; Qin, C.; Dong, Y.; Yu, H. Y.; Tam, K. C. Mass-Producible 3D Hair Structure-Editable Silk-Based Electronic Skin for Multiscenario Signal Monitoring and Emergency Alarming System. *Adv. Funct. Mater.* **2023**, *33*, No. 2305328.
(16) Li, S.; Zhang, Y.; Liang, X.; Wang, H.; Lu, H.; Zhu, M.; Wang, H.; Zhang, M.; Qiu, X.; Song, Y.; Zhang, Y. Humidity-Sensitive Chemoelectric Flexible Sensors Based on Metal-Air Redox Reaction for Health Management. *Nat. Commun.* **2022**, *13*, No. 5416.
(17) Jungst, T.; Smolan, W.; Schacht, K.; Scheibel, T.; Groll, J. Strategies and Molecular Design Criteria for 3D Printable Hydrogels. *Chem. Rev.* **2016**, *116*, 1496−1539.
(18) Keplinger, C.; Sun, J.-Y.; Foo, C. C.; Rothemund, P.; Whitesides, G. M.; Suo, Z. Stretchable, Transparent, Ionic Conductors. *Science* **2013**, *341*, 984−987.
(19) Yang, C.; Suo, Z. Hydrogel Ionotronics. *Nat. Rev. Mater.* **2018**, *3*, 125−142.
(20) Kong, W.; Wang, C.; Jia, C.; Kuang, Y.; Pastel, G.; Chen, C.; Chen, G.; He, S.; Huang, H.; Zhang, J.; Wang, S.; Hu, L. Muscle-Inspired Highly Anisotropic, Strong, Ion-Conductive Hydrogels. *Adv. Mater.* **2018**, *30*, No. 1801934.
(21) Yuk, H.; Lu, B.; Zhao, X. Hydrogel Bioelectronics. *Chem. Soc. Rev.* **2019**, *48*, 1642−1667.
(22) Zhu, Z.; Ling, S.; Yeo, J.; Zhao, S.; Tozzi, L.; Buehler, M. J.; Omenetto, F.; Li, C.; Kaplan, D. L. High-Strength, Durable All-Silk Fibroin Hydrogels with Versatile Processability toward Multifunctional Applications. *Adv. Funct. Mater.* **2018**, *28*, No. 1704757.
(23) Jeong, J.-W.; Shin, G.; Park, S. I.; Yu, K. J.; Xu, L.; Rogers, J. A. Soft Materials in Neuroengineering for Hard Problems in Neuroscience. *Neuron* **2015**, *86*, 175−186, DOI: 10.1016/j.neuron.2014.12.035.
(24) Cao, L.; Ye, C.; Zhang, H.; Yang, S.; Shan, Y.; Lv, Z.; Ren, J.; Ling, S. An Artificial Motion and Tactile Receptor Constructed by Hyperelastic Double Physically Cross-Linked Silk Fibroin Ionoelastomer. *Adv. Funct. Mater.* **2023**, *33*, No. 2301404.
(25) Cao, X.; Ye, C.; Cao, L.; Shan, Y.; Ren, J.; Ling, S. Biomimetic Spun Silk Ionotronic Fibers for Intelligent Discrimination of Motions and Tactile Stimuli. *Adv. Mater.* **2023**, *35*, No. 2300447.
(26) Xiao, Y.; Yang, Z.; Guo, B.; Wu, B.; Liu, R.; Zhang, S.; Zhao, P.; Ruan, J.; Lu, X.; Liu, K.; Chen, D. Strong and Tough Biofibers Designed by Dual Crosslinking for Sutures. *Adv. Funct. Mater.* **2023**, No. 2313131, DOI: 10.1002/adfm.202313131.
(27) Ding, H.; Liang, X.; Xu, J.; Tang, Z.; Li, Z.; Liang, R.; Sun, G. Hydrolyzed Hydrogels with Super Stretchability, High Strength, and Fast Self-Recovery for Flexible Sensors. *ACS Appl. Mater. Interfaces* **2021**, *13*, 22774−22784.
(28) Niu, Q.; Peng, Q.; Lu, L.; Fan, S.; Shao, H.; Zhang, H.; Wu, R.; Hsiao, B. S.; Zhang, Y. Single Molecular Layer of Silk Nanoribbon as Potential Basic Building Block of Silk Materials. *ACS Nano* **2018**, *12*, 11860−11870.
(29) Gan, D.; Han, L.; Wang, M.; Xing, W.; Xu, T.; Zhang, H.; Wang, K.; Fang, L.; Lu, X. Conductive and Tough Hydrogels Based on Biopolymer Molecular Templates for Controlling in Situ Formation of Polypyrrole Nanorods. *ACS Appl. Mater. Interfaces* **2018**, *10*, 36218−36228.
(30) Huang, L.; Du, X.; Fan, S.; Yang, G.; Shao, H.; Li, D.; Cao, C.; Zhu, Y.; Zhu, M.; Zhang, Y. Bacterial Cellulose Nanofibers Promote Stress and Fidelity of 3D-Printed Silk Based Hydrogel Scaffold with Hierarchical Pores. *Carbohydr. Polym.* **2019**, *221*, 146−156.
(31) Zhang, J.; Allardyce, B. J.; Rajkhowa, R.; Kalita, S.; Dilley, R. J.; Wang, X.; Liu, X. Silk Particles, Microfibres and Nanofibres: A Comparative Study of Their Functions in 3D Printing Hydrogel Scaffolds. *Mater. Sci. Eng., C* **2019**, *103*, No. 109784.
(32) Taddei, P.; Pavoni, E.; Tsukada, M. Stability toward Alkaline Hydrolysis of *B. Mori* Silk Fibroin Grafted with Methacrylamide. *J. Raman Spectrosc.* **2016**, *47*, 731−739.
(33) Shi, L.; Wang, F.; Zhu, W.; Xu, Z.; Fuchs, S.; Hilborn, J.; Zhu, L.; Ma, Q.; Wang, Y.; Weng, X.; Ossipov, D. A. Self-Healing Silk Fibroin-Based Hydrogel for Bone Regeneration: Dynamic Metal-Ligand Self-Assembly Approach. *Adv. Funct. Mater.* **2017**, *27*, No. 1700591.
(34) Iwai, K.; Uesugi, M.; Takemura, F. Tris(2,2′-Bipyridine)-Ruthenium(II)-Sensitized Photopolymerization of Acrylamide. *Polym. J.* **1985**, *17*, 1005−1011.
(35) Sun, G.; Huang, Y.; Ma, J.; Li, D.; Fan, Q.; Li, Y.; Shao, J. Photoinitiation Mechanisms and Photogelation Kinetics of Blue Light Induced Polymerization of Acrylamide with Bicomponent Photoinitiators. *J. Polym. Sci.* **2021**, *59*, 567−577.
(36) Barth, A. The Infrared Absorption of Amino Acid Side Chains. *Prog. Biophys. Mol. Biol.* **2000**, *74*, 141−173.
(37) Whittaker, J. L.; Choudhury, N. R.; Dutta, N. K.; Zannettino, A. Facile and Rapid Ruthenium Mediated Photo-Crosslinking of *Bombyx Mori* Silk Fibroin. *J. Mater. Chem. B* **2014**, *2*, 6259−6270.
(38) Guzman-Puyol, S.; Heredia-Guerrero, J. A.; Ceseracciu, L.; Hajiali, H.; Canale, C.; Scarpellini, A.; Cingolani, R.; Bayer, I. S.; Athanassiou, A.; Mele, E. Low-Cost and Effective Fabrication of Biocompatible Nanofibers from Silk and Cellulose-Rich Materials. *ACS Biomater. Sci. Eng.* **2016**, *2*, 526−534.
(39) Lacroix, M. R.; Gao, X.; Liu, Y.; Strauss, S. H. Unusually Sharp FTIR ν(OH) Bands and Very Weak O-H···F Hydrogen Bonds in $M_2(H_2O)_{1,2}B_{12}F_{12}$ Hydrates (M = Na-Cs). *J. Fluorine Chem.* **2019**, *217*, 105−108.
(40) Tang, J.; Chen, X.; Men, L.; Wang, Z. Effect of Fiber Geometry on Fracture and Fatigue of Composite Hydrogels. *J. Appl. Mech.* **2022**, *89*, No. 091006.
(41) Distler, T.; Boccaccini, A. R. 3D Printing of Electrically Conductive Hydrogels for Tissue Engineering and Biosensors − a Review. *Acta Biomater.* **2020**, *101*, 1−13.
(42) Wu, K.; Cui, Y.; Song, Y.; Ma, Z.; Wang, J.; Li, J.; Fei, T.; Zhang, T. Neuron-Inspired Self-Powered Hydrogels with Excellent Adhesion, Recyclability and Dual-Mode Output for Multifunctional Ionic Skin. *Adv. Funct. Mater.* **2023**, *33*, No. 2300239.
(43) Dobashi, Y.; Yao, D.; Petel, Y.; Tan Ngoc, N.; Sarwar, M. S.; Thabet, Y.; Ng, C. L. W.; Glitz, E. S.; Giao Tran Minh, N.; Plesse, C.; Vidal, F.; Michal, C. A.; Madden, J. D. W. Piezoionic Mechanoreceptors: Force-Induced Current Generation in Hydrogels. *Science* **2022**, *376*, 502−507.
(44) Zhang, X. H.; Sheng, N. N.; Wang, L. A.; Tan, Y. Q.; Liu, C. Z.; Xia, Y. Z.; Nie, Z. H.; Sui, K. Y. Supramolecular Nanofibrillar Hydrogels as Highly Stretchable, Elastic and Sensitive Ionic Sensors. *Mater. Horiz.* **2019**, *6*, 326−333.
(45) Zhou, Y.; Wan, C.; Yang, Y.; Yang, H.; Wang, S.; Dai, Z.; Ji, K.; Jiang, H.; Chen, X.; Long, Y. Highly Stretchable, Elastic, and Ionic Conductive Hydrogel for Artificial Soft Electronics. *Adv. Funct. Mater.* **2018**, *29*, No. 1806220, DOI: 10.1002/adfm.201806220.
(46) Jiang, H.; Ou, C.; Zhang, D.; Hu, X.; Ma, Y.; Wang, M.; Huang, Y.; Xiao, L. Tough Ion-Conductive Hydrogel with Anti-Dehydration as a Stretchable Strain Sensor for Gesture Recognition. *ACS Appl. Polym. Mater.* **2023**, *5*, 6828−6841.
(47) Liu, Y.-J.; Cao, W.-T.; Ma, M.-G.; Wan, P. Ultrasensitive Wearable Soft Strain Sensors of Conductive, Self-Healing, and Elastic

Hydrogels with Synergistic "Soft and Hard" Hybrid Networks. *ACS Appl. Mater. Interfaces* **2017**, *9*, 25559−25570.
(48) Wang, Z.; Chen, J.; Wang, L.; Gao, G.; Zhou, Y.; Wang, R.; Xu, T.; Yin, J.; Fu, J. Flexible and Wearable Strain Sensors Based on Tough and Self-Adhesive Ion Conducting Hydrogels. *J. Mater. Chem. B* **2019**, *7*, 24−29.
(49) Wang, Q.; Ran, X.; Wang, J.; Wang, S.; Zhang, P.; Gao, E.; Bai, B.; Zhang, J.; Zhou, G.; Lei, D. Elastic Fiber-Reinforced Silk Fibroin Scaffold with a Double-Crosslinking Network for Human Ear-Shaped Cartilage Regeneration. *Adv. Fiber Mater.* **2023**, *5*, 1008−1024.
(50) Niu, Q.; Huang, X.; Lv, S.; Yao, X.; Fan, S.; Zhang, Y. Natural Polymer-Based Bioabsorbable Conducting Wires for Implantable Bioelectronic Devices. *J. Mater. Chem. A* **2020**, *8*, 25323−25335.
(51) Das, S.; Pati, F.; Chameettachal, S.; Pahwa, S.; Ray, A. R.; Dhara, S.; Ghosh, S. Enhanced Redifferentiation of Chondrocytes on Microperiodic Silk/Gelatin Scaffolds: Toward Tailor-Made Tissue Engineering. *Biomacromolecules* **2013**, *14*, 311−321.
(52) Sultan, S.; Mathew, A. P. 3D Printed Scaffolds with Gradient Porosity Based on a Cellulose Nanocrystal Hydrogel. *Nanoscale* **2018**, *10*, 4421−4431.

https://doi.org/10.1021/acsbiomaterials.4c00201
ACS Biomater. Sci. Eng. 2024, 10, 3489−3499